

On Constraining A Transiting Exoplanet's Rotation Rate With Its Transit Spectrum

David S. Spiegel¹, Zoltán Haiman¹, B. Scott Gaudi²

¹*Department of Astronomy, Columbia University, 550 West 120th Street, New York, NY
10027*

²*Department of Astronomy, Ohio State University, 140 W. 18th Avenue, Columbus Ohio
43210-1173*

dave@astro.columbia.edu, zoltan@astro.columbia.edu,
gaudi@astronomy.ohio-state.edu

ABSTRACT

We investigate the effect of planetary rotation on the transit spectrum of an extrasolar giant planet. During ingress and egress, absorption features arising from the planet's atmosphere are Doppler shifted by of order the planet's rotational velocity ($\sim 1-2 \text{ km s}^{-1}$) relative to where they would be if the planet were not rotating. We focus in particular on the case of HD209458b, which ought to be at least as good a target as any other known transiting planet. For HD209458b, this shift should give rise to a small net centroid shift of $\sim 60 \text{ cm s}^{-1}$ on the stellar absorption lines. Using a detailed model of the transmission spectrum due to a rotating star transited by a rotating planet with an isothermal atmosphere, we simulate the effect of the planet's rotation on the shape of the spectral lines, and in particular on the magnitude of their width and centroid shift. We then use this simulation to determine the expected signal-to-noise ratio for distinguishing a rotating from a non-rotating planet, and assess how this S/N scales with various parameters of HD209458b. We find that with a 6 m telescope, an equatorial rotational velocity of $\sim 2 \text{ km s}^{-1}$ could be detected with a S/N ~ 5 by accumulating the signal over many transits over the course of several years. With a 30 m telescope, the time required to make such a detection reduces to less than 2 months.

Subject headings: astrobiology – planetary systems – radiative transfer – stars: atmospheres – stars:individual (HD209458) – astrochemistry

1. Introduction

Since the early 1990s, more than 200 planets have been discovered orbiting other stars. Roughly four fifths of the planets that have been discovered are at least half as massive as Jupiter, and about a quarter of the known planets orbit extremely close to their

parent star ($\lesssim 0.1$ AU). The Jupiter-mass planets that are in close orbits are highly irradiated by their stars and are therefore called “Hot Jupiters.” Twenty Hot Jupiters transit along the line of sight between Earth and their star (Charbonneau et al. 2000; Henry et al. 2000; Konacki et al. 2003; Bouchy et al. 2004; Pont et al. 2004; Konacki et al. 2004, 2005; Udalski et al. 2002a,b,c, 2003, 2004; Alonso et al. 2004; Bouchy et al. 2005b; McCullough et al. 2006; O’Donovan et al. 2006; Bakos et al. 2006; Collier Cameron et al. 2006; Burke et al. 2007; Gillon et al. 2007; Bakos et al. 2007b,a; Johns-Krull et al. 2007)¹. Observations of the transiting planets have confirmed their similarity to Jupiter by revealing that these are gas giant planets, with radii comparable to, or somewhat larger than Jupiter’s (Charbonneau et al. 2000; Henry et al. 2000; Gaudi 2005).

The effects of the tidal torques experienced by an orbiting body have been studied for a long time – for an early seminal analysis, see Goldreich & Peale (1966). Such torques tend to synchronize a satellite’s rotation rate to its orbital rate, and if the torque is sufficient this synchronization is achieved and the orbiter is said to be “tidally locked,” as the Earth’s Moon is. The Hot Jupiter-class extrasolar planets are thought to orbit sufficiently close to their stars that their tidal locking timescales are much shorter than the ages of the planets. The planets, then, are expected to be tidally locked to the stars, with one hemisphere in permanent day and the other in permanent night (Harrington et al. 2006).

A tidally locked Hot Jupiter will have a permanent sharp contrast in temperature between the substellar point and the night side, which must have a profound influence on the atmospheric dynamics. Showman & Guillot (2002) make simple predictions of the day/night temperature difference (~ 500 K) and the speed of winds (up to ~ 2 km s⁻¹), and their detailed, three-dimensional simulations agree with their estimates. Shallow-water simulations by Cho et al. (2003) predict longitudinally averaged zonal wind speeds of up to 400 m s⁻¹, with local winds approaching 2.7 km s⁻¹ (under some assumptions). Simulations by Cooper & Showman (2005) predict a super-rotational jet (i.e., blowing eastward, where north is defined by the right-hand rule) that blows the hottest part of the planet downstream by about 60° from the substellar point. Their simulations predict supersonic winds exceeding 9 km s⁻¹ at high latitudes, high in the atmosphere (where the optical depth is low) and winds exceeding 4 km s⁻¹ at pressures near the photosphere. A Spitzer Space Telescope phase curve for *v* Andromedae b rules out a phase-shift as large as 60° between the substellar point and the hottest spot (Harrington et al. 2006), but a Spitzer phase curve for HD189733b favors a $\sim 30^\circ$ shift for that planet (Knutson et al. 2007a), so it remains unclear to what extent available data indicate very strong photospheric winds.

Transmission spectroscopy is a way to probe the atmospheres of these planets. Charbonneau et al. (2002) were the first to detect an absorption feature in what is probably the atmosphere of HD209458b, when they found that the effective radius of the planet increases slightly at the

¹Corot-Exo-1b is reported at http://www.esa.int/esaCP/SEMCKNU681F_index_0.html.

wavelength of a strong sodium absorption doublet (the sodium D lines) at ~ 590 nm. In addition, Vidal-Madjar et al. (2003, 2004) have reported a number of absorption features in HD209458’s transit spectra that are due to various species (including hydrogen Lyman alpha, neutral carbon, oxygen, and sulfur, and some ionization states of carbon, nitrogen, and silicon) in a hot exosphere that is probably only loosely bound to the planet. Intriguingly, through analyzing the red and near-IR portion of HD209458b’s transit spectrum Barman (2007) found a 10σ detection of atmospheric water vapor. Several measurements of the planet’s emission spectrum, however, have found results that seem to be inconsistent with high water abundance high in the atmosphere (Grillmair et al. 2007; Richardson et al. 2007; Swain et al. 2007).

Initial work by Seager & Sasselov (2000) and a comprehensive study by Brown (2001, hereafter B01) have described various other considerations that should affect the details of transit spectra, including the orbital motion of a planet (a few tens of kilometers per second in the radial direction), the rotation of the planet (a few kilometers per second at the equator, according to the hypothesis that the planet is tidally locked), and winds on the planet’s surface (in B01’s analysis, up to ~ 1 km s $^{-1}$). These physical effects should tend to broaden or impose Doppler shifts on absorption features due to the planet’s atmosphere. B01 constructed an impressively detailed model of radiative transfer through a Hot Jupiter’s atmosphere, assuming various models of zonal windflow superimposed on an equatorial bulk rotation speed of $v_{\text{eq}} = 2$ km s $^{-1}$, which is approximately the value for HD209458b under the assumption that it is tidally locked in its 3.5 day orbit. He finds the height of the cloud deck to be the most important parameter that affects the transmission of light through the planet’s atmosphere.

The original discovery of the roughly Jupiter-mass planet in a close, ~ 4 day orbit around 51 Pegasi (Mayor & Queloz 1995) prompted interest in the dynamics and structure that must govern a highly insolated gas giant planet (Guillot et al. 1996). Observations of the transiting Hot Jupiters heightened this interest when they revealed a puzzling feature of these planets: at least several of them are a bit puffier than Jupiter, with diameters ranging from slightly larger than Jupiter’s to as much as $\sim 80\%$ larger. It is not clear what allows some planets to maintain such large radii. It has been suggested that if a Jovian planet migrates very quickly, from its presumed formation location at least several AU from its star, to its eventual several day orbit, then it might reach its final home before it has cooled enough to shrink to Jupiter’s radius. Accordingly, some authors have investigated the migration processes that lead gas giant planets to such close orbits as have been found (e.g. Trilling et al. 2002). Others have investigated various ways in which a gas giant could either be heated once it ends up near its star, or otherwise maintain sufficient internal energy to sustain its inflated size (Guillot & Showman 2002; Burrows et al. 2003; Laughlin et al. 2005; Bodenheimer et al. 2003; Guillot 2005; Burrows et al. 2007; Chabrier & Baraffe 2007). Although various physical mechanisms have been suggested as the apparently missing energy source that allows the unexpectedly large radii sometimes seen, the lesson of these investiga-

tions *in toto* is that it is not easy to explain the inflated sizes, either in terms of the greater stellar flux that these planets experience by virtue of being so close to their stars, or in terms of their evolutionary migratory histories. A recent paper by Winn & Holman (2005) propose that, contrary to the commonly accepted paradigm, Hot Jupiters might be trapped in a Cassini state with large obliquity, in which the spin–axis precesses in resonance with the orbit, but lies nearly in the orbital plane. Such a state might be stable against perturbation, and yet able to generate sufficient internal energy to increase a gas giant planet’s radius to the observed values. In light of an even more recent analysis by Levrard et al. (2007), however, it appears that the probability of capture into a Cassini state 2 resonance is quite small for a planet with semi–major axis $a < 0.1$ AU. Furthermore, Fabrycky et al. (2007) argue that even if a planet is captured into Cassini state 2, it is likely to remain there for a time that is short relative to the age of the system.

High–resolution transit spectra that have high signal–to–noise ratios will allow us to distinguish between various models of orbit, rotation, and weather, as discussed by B01. Because the orbit is known to high accuracy, and the predictions of the effects of weather (or climate) are highly uncertain, as described above, we will focus in this paper on the much more easily predicted effect of a planet’s rotation on a transit–spectrum. If we neglect winds, then the large–obliquity Cassini state described by Winn & Holman (2005) should have a spectral signature that is very similar to that of a non–rotating model. In contrast, the rotation of a tidally locked planet should impose a Doppler distortion on spectral lines arising from the planet’s atmosphere that is roughly an overall redshift during ingress, as the planet is just entering the stellar disk, and a similar distortion that is roughly an overall blueshift during egress, as the planet is just exiting the disk. During mid–transit, the spectral distortion is more similar to rotational broadening. In the present investigation, we address whether there is any hope that these spectral distortions from tidally–locked rotation can be observed. In our study, we focus only on the sodium doublet detected by Charbonneau et al. (2002). As we will show below, the sensitivity of a measurement of rotation scales with the square root of the number of lines under consideration. Model spectra from, e.g., Sudarsky et al. (2003) and Barman (2007) predict a strong potassium doublet at ~ 770 nm, strong water absorption features in the near–infrared, and a handful of near–UV lines. If some of these are confirmed in the atmosphere of a transiting planet, they will provide a modest increase in S/N. Since the sodium lines are expected to be the strongest, however, it seems unlikely that observing multiple lines will yield a boost in S/N by more than a factor of a few.

We emphasize that it may not be at all justified to neglect winds. It is quite likely that there are super–rotational winds on Hot Jupiters, which are probably necessary to heat the “night” side. As indicated above, some models predict, and the observed phase curve for HD189733b suggests, that at the photosphere these winds might be significantly (100% or more) greater than the equatorial rotation rate, and therefore might contribute importantly to the Doppler distortion induced by the motion of the planet’s atmosphere. Nevertheless,

in order to isolate the contribution of rotation, we do neglect winds in this study. The Doppler distortions that we predict can therefore probably be taken as a lower bound on the distortions that would be observed for a tidally–locked transiting Hot Jupiter.

We find that the spectral shifts induced by rotation will be difficult to detect with current technology, but perhaps not insurmountably so, at least with technology that might be available in the not–to–distant future. The measurements we will describe are limited by a paucity of photons. As such, their signal–to–noise ratio will be enhanced by a bright star and a puffy planet (i.e., a planet with a large scale–height). HD209458 is at least a magnitude brighter than any other star with a known transiting planet except HD189733, and its planet is larger than HD189733b; so HD209458b should be a better target than any other known transiting planet except possibly HD189733b. In this paper, we model the HD209458b system because it is the best–studied system, and it is unlikely that any currently–known planets would be significantly better targets. In a single transit, observations of HD209458 with a 6 m telescope that has a high–resolution ($> 50,000$) optical spectrograph with good throughput ($\sim 18\%$) could only show the influence of tidally locked rotation at the $\sim 0.2\sigma$ level. With ultrahigh–resolution ($\gtrsim 700,000$) and good throughput ($\sim 4\%$) this effect would still only show up at the $\sim 0.6\sigma$ level. In less than a year, the signal of rotation could be present at five times the noise ($S/N = 5$). Of course, a telescope with larger collecting area, higher spectral resolution, or better throughput would cause the signal to be apparent at that significance level in less time.

Other studies have approached the problem of determining the rotation rate from a different angle. Seager & Hui (2002) and Barnes & Fortney (2003) suggest that an oblate spheroid will have a different transit light curve from a perfect sphere, and so measuring the oblateness from transit photometry will provide a handle on the rotation rate. The oblateness is somewhat degenerate with several other parameters that are not perfectly known, however, so they conclude that it would be difficult to actually determine that rotation rate in this manner. The method we describe here could eventually prove to be an important complement to other observations to constrain the rotation rate.

In the remainder of this paper, we address this idea in detail. One complication that we discuss below is that the technique of this paper is not immune from several near–degeneracies among the many attributes of transiting extrasolar planets that influence light curves or spectra. Although it is likely that current or near–future instruments will be sensitive enough that the spectral distortion imposed by HD209458b’s rotation (if it is tidally locked) is visible, it might still be very challenging to discern the fingerprint of rotation from other attributes that affect the spectra at a similar level. In this paper, we tackle the forward problem of calculating the amount of distortion that is caused by rotation. The inverse problem – determining from observations whether a planet is tidally locked – is more difficult and should be the topic of a future study.

The structure of the rest of this paper is as follows: In § 2, we describe qualitatively what

happens to the starlight received on Earth when a planet transits its star; we give a rough order of magnitude estimate of the the magnitude and detectability of the spectral distortions caused by tidally locked rotation; and we briefly describe some technological progress and remaining challenges relevant to our task of deducing bulk motions in a planet’s atmosphere from transit spectra. In § 3, we describe our computational model of a transit spectrum. In § 4, we describe the results of our model according to various assumed input parameters. In § 5, we discuss the scaling of S/N on various model parameters and we address the prospects of actually observationally determining whether a transiting planet is tidally locked. In § 6, we conclude by describing various ways to boost our predicted S/N to a more optimistic value.

2. Overview of the Problem

The practical feasibility of the investigation we undertake depends on a few factors: understanding the various detailed processes that affect the starlight that reaches Earth when a planet transits its star; the magnitude of the distortion that tidally locked rotation induces; and the technology available to measure such distortions. In this section, we give an overview of these three factors – in particular, in § 2.2, we give a simple estimate of the results that we will later (in § 4) calculate in detail.

2.1. Relevant Processes

A planet transiting in front of its star affects the starlight that ultimately reaches Earth in many ways. The motion of the planet’s atmosphere (rotation and winds) is a small perturbation on top of several more dominant effects. We therefore summarize below the physical processes that are at least as significant as the effect of tidally locked rotation. Figure 1 schematically represents this situation, and captures nearly all of the processes described below: a rotating planet (of exaggerated relative size) transits in front of a rotating star. The figure depicts a snapshot partway through ingress, when half of the planet is in front of the stellar disk². The white circle indicates a hypothetical sharp demarcation between the opaque part of the planet (in black) and the optically thin part, labeled “Atmosphere” (described further below).

1. *Geometric Occultation:*

The largest effect is an overall dimming by a factor of roughly the ratio of the area of the planet to that of the star: $(R_p/R_*)^2$. Since stars are not perfectly uniform disks,

²The planet is above the star’s equator to represent a slight inclination in its orbit.

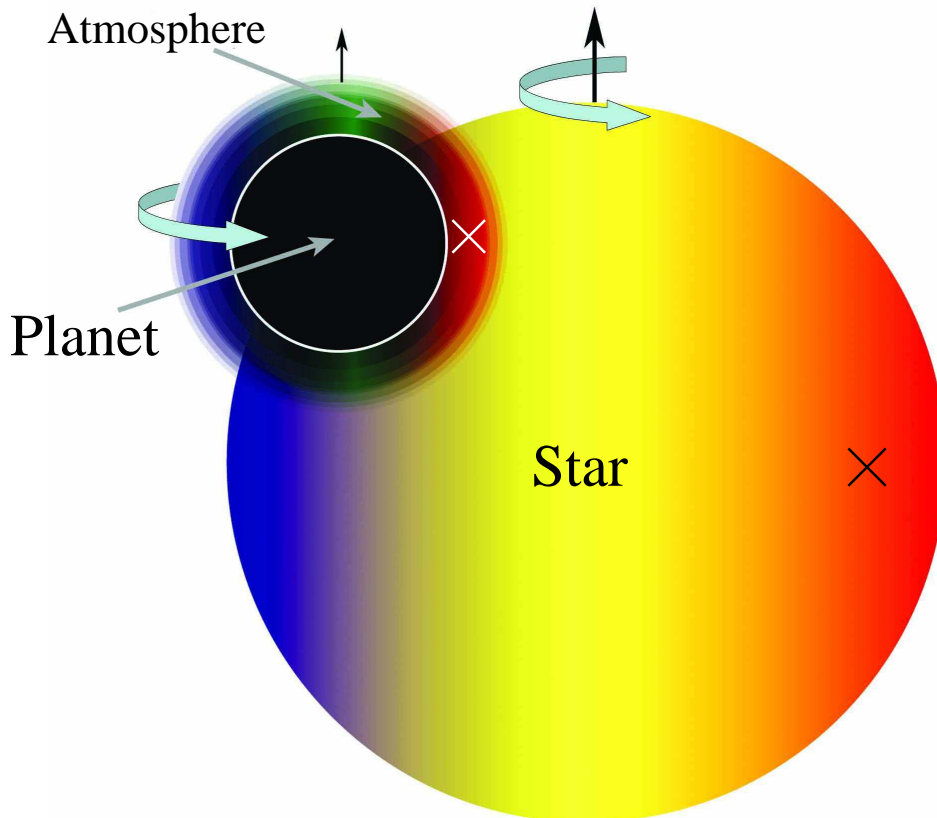


Fig. 1.— Rotating planet beginning to transit in front of rotating star. The vertical black arrows represent the rotation axes of the planet and the star, and the curved arrows indicate the direction of rotation for each. The X’s on the right–sides of both the planet and the star indicate regions that are receding from the observer and are therefore redshifted; the unmarked left sides of the planet and the star are moving toward the observer and are therefore blueshifted. The white circle surrounding the opaque black part of the planet denotes the cloud deck, or the boundary between the partially transparent and the fully opaque portions of the planet’s disk. The planet is orbiting in the same sense as both it and the star are rotating. The planet is shown above the star’s midplane to represent the inclination of the orbit relative to the line–of–sight.

but instead tend to darken toward the limb at most visible wavelengths, the fractional dimming due to being in the planet’s shadow tends to be slightly less than the ratio of the areas when the planet is near the edge of the stellar disk and slightly more than this ratio when the planet is near the center.

2. *Stellar Wobble:*

The primary spectral effect of the planet orbiting the star is the radial velocity wobble induced by the planet’s gravity. This periodic spectral shift is of course in effect during the transit, when, for a close–in planet like HD209458b, it has an influence on the order

of $\sim \pm 10 \text{ m s}^{-1}$. This effect is a redshift as the planet begins to transit across the disk (during ingress) and a blueshift during egress.

3. *Rossiter–McLaughlin Effect:*

A more subtle effect arises because, during the transit, the planet moves across – and therefore blocks – parts of the star that have different recessional velocities. If (as is expected) the planet’s orbit is aligned with the star’s spin, then during ingress the planet is blocking a part of the star that is slightly blueshifted, and during egress it is blocking a part of the star that is slightly redshifted. Figure 1 illustrates the planet blocking some of the bluest parts of the star during ingress.

The parts of the star that are occluded during ingress/egress have spectra that are blue/redshifted by a velocity that is approximately the equatorial rotational speed of the star, or about $\sim 1\text{-}2 \text{ km s}^{-1}$ for a Sun-like star. As the figure indicates, during ingress/egress, the integrated spectrum of the remaining (unblocked) parts of the star is on average slightly redder/bluer than it would be if the planet were entirely transparent. Therefore, during ingress, the centroids of stellar lines are shifted slightly to the red, and during egress the centroids are correspondingly shifted to the blue.

This so-called Rossiter–McLaughlin effect (RME), described originally by Rossiter (1924) and McLaughlin (1924) in the case of eclipsing binary stars, adds to the shifts already caused by the radial velocity induced by the planet’s gravity, described in (2.) above. The RME has been described in depth more recently in the context of extrasolar planets by Ohta et al. (2005), Giménez (2006), and Gaudi & Winn (2007). These centroid-shifts are expected to be comparable in magnitude to the radial velocity wobble from the planet’s gravity, and can be roughly estimated as

$$|\delta v_{\text{R-M}}| \sim 1 \text{ km s}^{-1} \times (R_p/R_*)^2 \sim 10 \text{ m s}^{-1},$$

In fact, the amount of the shift can be predicted precisely for a given orientation of the planet’s orbit, and so measuring the shift is tantamount to measuring the alignment between the star’s spin and the planet’s orbit. Three years ago, Winn et al. (2005) first found that the spin of HD209458 and the orbital plane of its planet are nearly aligned. The degree of alignment has been measured for two other systems – Winn et al. (2006) found that the spin of HD189733 and its planet are also nearly aligned, and Narita et al. (2007) measured a mis-alignment between these two vectors by $\sim (30 \pm 20)^\circ$ in the TrES-1 system.

4. *Planet’s Atmospheric Opacity:*

Furthermore, a gas-giant planet’s opacity surely does not have a perfectly sharp discontinuity at an outer boundary, as a billiard ball does. Instead, it has an extended atmosphere in which the opacity must vary more or less smoothly. There may be a cloud layer, below which the planet is entirely opaque to tangential rays and above which the opacity varies smoothly. Most critical to our investigation, at a given radius,

the planet’s opacity to tangential lines of sight must vary with wavelength, depending on the contents of its atmosphere. At wavelengths of strong atomic or molecular transitions, the planet’s atmosphere will be more opaque than at other wavelengths. As a result, the effective radius of the planet, or the radius at which the optical depth along a tangential ray is of order unity, is greater at some wavelengths than at others. These effects have been described in detail by B01.

5. *Planet’s Orbital Motion:*

The motion of the planet’s atmosphere must influence the transit spectrum in several delicate ways. As B01 points out, there are three main mechanisms by which the motion of a planet’s atmosphere relative to its star can affect the spectrum: the planet’s orbital velocity along the line-of-sight, the planet’s (possibly tidally locked) rotation, and winds in its atmosphere. The largest effect of these three is the orbital velocity, which imposes a bulk blue/redshift during ingress/egress of $\sim 15 \text{ km s}^{-1}$ to spectral lines arising from the planet’s atmosphere. These shifts are of opposite sign to the radial velocity wobble and to the shifts from the RME, and therefore tend to lessen the apparent RME slightly.

6. *Planet’s Atmospheric Motion:*

The most dynamically interesting (and subtlest) effects are those caused by the planetary rotational velocity and atmospheric winds. Since a tidally locked planet rotates in the same sense as it orbits, the rotational velocity of its outside edge has the same sign as its orbital velocity, and the rotational velocity of its inside edge has the opposite sign. As a result, during the beginning of ingress and the end of egress, when only the inside edge of the planet is over the star, tidally locked rotation will impose a spectral distortion that is in the opposite sense of that caused by the bulk orbital velocity described in (5.) above, and that is in the same sense as the RME: the distortions are roughly equivalent to a relative redshift during ingress (graphically represented in Figure 1) and a relative blueshift during egress. During mid-transit, with some parts of the rotating planet’s atmosphere moving toward and other parts away from the star relative to an otherwise identical but non-rotating planet, the overall influence of the planet’s rotation is approximately equivalent to rotational broadening.

Winds complicate the picture even further. It is likely that winds tend to rush from the substellar hot spot to the colder night side of the planet. With the substellar point on the opposite side of the planet from Earth during a transit, this corresponds to winds rushing toward us at several hundred to several thousand meters per second. This would tend to blueshift the spectrum throughout the transit. Zonal wind bands, somewhat similar to those on Jupiter but with much higher speeds, or other more detailed winds, can have an even more intricate effect.

7. *Additional Effects:*

If a transiting planet were to have nonzero orbital eccentricity, or rings, these could

complicate a measurement of rotation rate. Nonzero eccentricity would break the symmetry between ingress and egress. Still, if the orbit were well-known, this could be modeled and taken into account. It seems unlikely that a Hot Jupiter could maintain rings: Icy rings would sublimate, and, if not continuously replenished, dusty/rocky rings would quickly succumb to the Poynting–Robertson effect (Poynting 1903; Robertson 1937). But if, somehow, a ring were to find a way to persevere around a transiting Hot Jupiter, it could confound – perhaps hopelessly – a measurement of rotation. The consequences of rings for the Rossiter–McLaughlin effect is addressed in Ohta et al. (2006). Saturn’s rings are nearly four–times the area of the planet, so for a planet (with equatorial rings that are as relatively large as Saturn’s) whose orbit is tilted an angle 0.1 (in radians) from edge-on, the rings would be $\sim 40\%$ the area of the planet, which would increase the RME by $\sim 40\%$. Uncertainty about the presence and size of a ring introduces an uncertainty in the size of the RME effect that is probably larger than the size of the rotation effect. Furthermore, a ring would occlude a (small) part of the planet’s atmosphere, which would (slightly) reduce the strength of the rotation signal.

Other interesting phenomena that primarily affect a transit light curve, rather than the spectrum, include star–spots (Silva 2003), atmospheric lensing (Hui & Seager 2002), and finite–speed–of–light effects (Loeb 2005). Although Winn & Holman (2005) describe a possible configuration (Cassini state 2) that would produce a spectral signature that is nearly identical to what would be expected from a non–rotating planet, the likelihood that any Hot Jupiters are in such a configuration might be low, and it seems quite likely that *some* transiting planets are not in this state. Nonetheless, the motion of a transiting planet’s atmosphere – rotational, wind, or other – is clearly interesting, and the basic technique that we describe below is applicable to any model of atmospheric motion.

2.2. Preview of Results

A rough estimate of the velocity–shift that is imposed during ingress to the centroids of the stellar Na D–lines by the planet’s tidally locked rotation (on top of the RME and the shift from the planet’s orbital velocity, both of which would be present even if the planet were not rotating) is the following:

$$\begin{aligned} \delta v &\sim \left(\langle \cos[\phi] \rangle_{-\pi/2}^{\pi/2} \right) \times \left(\frac{1}{2} \times \frac{R_p^2}{R_*^2} \right) \times \left(\frac{2\pi R_p \Pi_{\text{atm}}}{\pi R_p^2} \right) \times v_{\text{eq}} \\ &\sim 0.64 \times 1\% \times 15\% \times 2000 \text{ m s}^{-1} \\ &= 1.9 \text{ m s}^{-1}. \end{aligned} \tag{1}$$

In this equation, ϕ is a planet–centered azimuthal angle, R_p and R_* are the planet’s and star’s radius, respectively, Π_{atm} is the height of the planet’s atmosphere, and v_{eq} is the equatorial

rotation speed. The rotation speed at angle ϕ is $v_{\text{eq}} \cos[\phi]$. We take the average of $\cos[\phi]$ from $-\pi/2$ to $\pi/2$ to get the average planetary rotation speed. We have used $\Pi_{\text{atm}} = 7500$ km, or 15 times the presumed scale height of 500 km, because the sodium lines are so heavily saturated that at the assumed abundance and cloud deck height in our model the line cores do not become optically thin until that height. Burrows et al. (2004) and Fortney (2005) describe how the optical depth along tangential rays is greater than the optical depth on normal rays. The product

$$\delta_{\text{atm}} \approx \left(\frac{1}{2} \times \frac{R_p^2}{R_*^2} \right) \left(\frac{2\pi R_p \Pi_{\text{atm}}}{\pi R_p^2} \right) = \left(\frac{R_p}{R_*} \right)^2 \left(\frac{\Pi_{\text{atm}}}{R_p} \right)$$

is the ratio of the area of the portion of the planet’s atmosphere that is in front of the star halfway through ingress to the total area of the disk of the star. Based on this estimate, we expect a maximum velocity shift of $\delta v \sim 190 \text{ cm s}^{-1}$. If we take into account that HD209458b’s orbit is actually slightly inclined relative to the line of sight, the cosine average decreases to ~ 0.45 , and the total estimate decreases to $\sim 140 \text{ cm s}^{-1}$. This estimate is in reasonably good agreement with the centroid–shifts predicted by the full model calculation below ($\sim 60 \text{ cm s}^{-1}$); the difference between the estimates is most likely due to the difference between the shapes of the stellar and planetary lines.

We now estimate the signal–to–noise ratio for the detectability of this effect in an observation of duration Δt , with a telescope that has diameter D and throughput efficiency η . The signal is the distortion of the spectrum relative to a non–rotating planet, and for now we will assume that the noise is dominated by photon noise. If a spectrum $F[\lambda]$ with a symmetric absorption feature of depth ΔF centered at λ_0 is redshifted by an amount $\Delta\lambda$ to $\widehat{F}[\lambda] \equiv F[\lambda - \Delta\lambda]$, what is the integrated absolute difference $|F - \widehat{F}|$ over some wavelength range $2L$ centered on λ_0 ? If the absorption feature is wide compared with $\Delta\lambda$, then, by symmetry,

$$\begin{aligned} S &= \int_{\lambda_0-L}^{\lambda_0+L} |F[\lambda] - F[\lambda - \Delta\lambda]| d\lambda \\ &\approx 2 \int_{\lambda_0}^{\lambda_0+L} (F[\lambda] - F[\lambda - \Delta\lambda]) d\lambda; \end{aligned} \quad (2)$$

and if $\Delta\lambda$ is small then

$$\begin{aligned} S &\approx 2\Delta\lambda \int_{\lambda_0}^{\lambda_0+L} F'[\lambda] d\lambda \\ &\approx 2(\Delta\lambda)(\Delta F). \end{aligned} \quad (3)$$

We may now estimate the S/N of our effect (for a single absorption line) using the lesson of equation (3), provided we know the absolute normalization of the stellar spectrum (the number of photons per unit wavelength). A spherical blackbody of radius R_* and

temperature T_* , at distance d from the telescope, has a photon number flux at wavelength λ of

$$\begin{aligned} \frac{d\dot{N}_\gamma}{d\lambda} &\sim B_\lambda[\lambda, T] \left(\frac{1}{hc/\lambda} \right) \left(\frac{\pi R_*^2}{d^2} \right) \times \eta \pi (D/2)^2 \\ &= \frac{\pi^2 c}{2\lambda^4 (\exp[(hc)/(\lambda k T_*)] - 1)} \times \eta \left(\frac{R_* D}{d} \right)^2, \end{aligned} \quad (4)$$

where B_λ is the Planck function. Since the fractional decrease in the spectrum at the line-center is approximately δ_{atm} , we may express the parameter ΔF from equation (3) as $\Delta F \approx \delta_{\text{atm}} (d\dot{N}_\gamma/d\lambda)$. Similarly, since the root-mean-square velocity shift during ingress is $\langle v^2 \rangle^{1/2} \sim (1/2) \times (2000 \text{ m s}^{-1}) = 1000 \text{ m s}^{-1}$,³ we may express the parameter $\Delta\lambda$ as $\Delta\lambda \sim (\langle v^2 \rangle^{1/2}/c) \times \lambda_0$. The distortion (the signal) from a single line can therefore be estimated as

$$\begin{aligned} S &= \delta N_\gamma \sim 2(\Delta\lambda) \left(\delta_{\text{atm}} \frac{d\dot{N}_\gamma}{d\lambda} \right) \Delta t \\ &= \frac{\pi^2 c (\delta_{\text{atm}}) \Delta\lambda}{\lambda^4 (\exp[(hc)/(\lambda k T_*)] - 1)} \times \eta \left(\frac{R_* D}{d} \right)^2 (\Delta t). \end{aligned} \quad (5)$$

The shot-noise is the square root of the number of photons in a wavelength range $2L$ roughly equal to the FWHM of the line, or about 7 km s^{-1} for a heavily saturated line such as the Na D lines under consideration:

$$\begin{aligned} N &\sim \sqrt{\frac{d\dot{N}_\gamma}{d\lambda} (2L) (\Delta t)} \\ &\sim \sqrt{\frac{\pi^2 L c (\Delta t)}{\lambda^4 (\exp[(hc)/(\lambda k T_*)] - 1)}} \times \sqrt{\eta} \left(\frac{R_* D}{d} \right). \end{aligned} \quad (6)$$

We estimate the total signal-to-noise ratio arising from a single absorption line, during an ingress integration of duration Δt , to be roughly

$$\begin{aligned} S/N &\sim \frac{\pi (\delta_{\text{atm}})}{\sqrt{\exp[(hc)/(\lambda k T_*)] - 1}} \left(\frac{\Delta\lambda}{\lambda} \right) \left(\sqrt{\frac{c\Delta t}{L}} \right) \left(\frac{R_* D}{d\lambda} \right) \sqrt{\eta} \\ &\sim (6.6 \times 10^{-4}) (3.3 \times 10^{-6}) (2.1 \times 10^{11}) (5.0 \times 10^{-3}) \sqrt{\eta} \\ &\sim 2.3 \sqrt{\eta}. \end{aligned} \quad (7)$$

The above calculation uses parameters for HD209458 and its planet, a sodium D line, and a 6 m telescope: $\lambda = 600 \text{ nm}$; $\Delta t = 1000 \text{ s}$; $R_* = 7.3 \times 10^{10} \text{ cm}$; $T_* = 6100 \text{ K}$, $d = 47 \text{ pc}$; and $D = 600 \text{ cm}$. For two identical absorption lines, we gain a factor of $2^{1/2}$ in S/N, and for

³We write $(1/2) \times (2000 \text{ m s}^{-1})$ because the mean value of \cos^2 from $-\pi/2$ to $\pi/2$ is $1/2$

gress we gain another factor of $2^{1/2}$, giving a total one–transit S/N of roughly $4.6\eta^{1/2}$, not counting the additional signal available during mid–transit (see further discussion below). This S/N ratio is in principle independent of the spectral resolution of the spectrograph, for sufficiently high spectral resolution. For low spectral resolution, however, the S/N could be lower than this estimate (below, we conclude that the S/N loses its dependence on resolving power for spectral resolution $\gtrsim 500,000$).

There were several optimistic assumptions that went into this estimate. Still, this rough estimate of the degree to which a planet’s rotation influences its transit spectrum indicates that the more in–depth study that we perform below is warranted.

2.3. Available Technology

Detecting the centroid–shifts caused by tidally locked rotation ($\lesssim 1 \text{ m s}^{-1}$) will require very precise measurements of stellar transit spectra. Obtaining such high precision spectra will be quite challenging, for a number of reasons, several of which were described in the groundbreaking paper by Butler et al. (1996) that analyzes the limits of Doppler precision. Of particular concern, stellar pulsations and turbulent motions in stellar photospheres can cause small regions of the stellar disk to move at up to 300 m s^{-1} (Dravins 1985; Ulrich 1991). These motions tend to average out to produce stellar spectra that are largely stable; but it is likely that at least some giant convection cells are not small relative to the size of a planet, and these could introduce a contaminating source of noise when they are located behind the planet or its atmosphere. Butler et al. (1996) reviewed what was then known about the variability of stellar line–profiles; the upshot is that line–widths may vary by up to several meters per second over several years, but it is not clear to what extent spurious apparent velocity shifts may be induced by convection, and such stellar jitters may prove to be a significant source of noise that would render it difficult to measure sub meter–per–second velocity–shifts. More recently, Bouchy et al. (2005a) have actually achieved sub meter–per–second accuracy with the HARPS instrument (spectral resolution of 115,000), and they have found a dispersion in night–averaged radial velocity measurements for a particular star (HD160691) of $\sim 0.4 \text{ cm s}^{-1}$ for nights when they took many ($\gtrsim 200$) observations. Since in our situation (taking spectra during ingress, say) we have minutes, not hours, available, the rms scatter in ingress–averaged radial velocity measurements is likely to be larger than what they found. In addition to the difficulties posed by several systematic sources of noise, achieving sufficient photon statistics will be difficult for two reasons: for a given throughput efficiency η , higher spectral resolution means fewer photons per bin; and η tends to decrease with increasing spectral resolution R_S .

By the mid–1990s, the timeless quest for high–resolution spectrographs reached a milestone at the Anglo–Australian Telescope with the development of UHRF and its resolving power of up to 1,000,000 (Diego et al. 1995). Despite impressive throughput relative to

previous endeavors, however, its efficiency was insufficient to obtain the sub decameter-per-second Doppler precision on a $V \geq 7$ star that would be required for planet searches. With a $R_S = 600,000$ spectrograph built at Steward Observatory, Ge et al. (2002) obtained stellar spectra with $R_S \sim 250,000$ and throughput of 0.8%. Furthermore, they predicted that by optimizing their technology they could increase the throughput to 4%. More recently, Ge et al. (2006) detected a new planet, around HD 102195, with the Exoplanet Tracker instrument at Kitt Peak. This instrument has resolution of $R_S \sim 60,000$ and total throughput of 18%. Plans for a spectrograph that has resolving power of 120,000 on a thirty meter telescope (Tokunaga et al. 2006) give cause for optimism that increased aperture area and efficiency feeding high and ultrahigh-resolution spectrographs will, in coming years, provide accurate enough spectra that tidally locked rotation of HD209458b has a detectable influence.

3. A Model of a Planetary Transit

We consider the spectrum of a star whose companion planet transits across the face of the stellar disk from Earth’s perspective. The primary effect of the planet is to reduce the stellar flux at all wavelengths, but the planet’s chemical composition, internal structure, and rotation rate influence the spectrum in wavelength-dependent ways. Since each of these factors – and others too, such as the star’s rotation – influences the observed spectrum, we built a model that incorporates the many parameters related to each process. The star and the planet are both assumed to rotate as solid bodies, with no other (nonthermal) motion in their atmospheres. Since deviations from pure solid body rotation are likely to be no more than 25% over the disk of the star – e.g., the Sun’s equator-to-pole variation in rotation rate is about 21%, as per Howard et al. (1984), this is probably a reasonable assumption for the star. For the planet, this assumption might fail, because wind-speeds in excess of the equatorial rotation speed of $v_{\text{eq}} \approx 2 \text{ km s}^{-1}$ are predicted by many models, as described in § 1 above. Still, when making this initial study of the spectral effect of the motion of a transiting planet’s atmosphere, separating rotation from other processes makes the problem more tractable. We set parameter values to match measured values from the HD209458b system where possible.

The planet is modeled as an inner component that is entirely opaque and an outer component that is isothermal and drops off exponentially. We compute the wavelength-dependent optical depth due to the sodium D-doublet at $\approx 590 \text{ nm}$ in the planet’s atmosphere; important parameters include the temperature and density of the planet’s atmosphere and its Na-content. We use the Voigt profile – as described by, e.g., Press & Rybicki (1993) – to calculate $\tau[\lambda]$, the optical depth to absorption along the line of sight.

As the planet transits the star, there are four points of “contact” between the planet and the star (really between their projections on the sky): when the disk of the planet first touches the disk of the star; when the planet is first entirely over the stellar disk; when the

planet is last entirely over the stellar disk; and when the planet last touches the stellar disk. We will additionally sometimes refer to “1.5th” contact (half-way between first and second contact), and analogously to “2.5th” and “3.5th” contact.

As described in § 2 above, the type of distortion that a planet’s rotation imposes relative to a non-rotating planet changes depending on when during the transit the observation is made. During ingress or egress, the rotation of a tidally locked planet’s atmosphere will impose a distortion similar to an overall shift relative to a non-rotating planet: redshift during ingress; blueshift during egress. When the planet is in mid-transit, in the middle of the stellar disk, the overall distortion to the spectrum imposed by its rotation is akin to a star’s rotational broadening. Since the line-centers of the lines we are considering are heavily saturated and therefore flat at their cores, rotational broadening has the somewhat counterintuitive effect of steepening the cores of the profiles while broadening the wings. We will discuss this in greater detail in the next section. Although the type of distortion is different during ingress and egress from during mid-transit, it turns out that the amount of distortion, in terms of S/N ratio, is nearly constant throughout transit. This, too, we will discuss in § 4 below.

We simulate the HD209458b system, with a $1.32R_J$ planet in a 3.5 day orbit, orbiting a G0 star at with radius $1.05R_\odot$ that is 47 pc away. Our model star has the limb darkening profile that Knutson et al. (2007b) measured for HD209458. In order to approximate the fits to the data in Charbonneau et al. (2002), we assign our model planet’s atmosphere a sodium-content and cloud deck height (1% solar, and 0.01 bars) that are comparable to the parameter-combinations that result in the best fits in that paper. Finally, we present results at our simulation’s spectral resolution ($R_S = 700,000$), and we simulate transit events observed using two different lower resolution spectrographs, one with spectral resolution $R'_S = 50,000$ and one with $R'_S = 150,000$. All spectrographs (and associated optical paths) in our simulations have 100% throughput efficiency. In the remainder of this section, we provide a detailed description of our parameterization of the problem.

3.1. Parameters of the Star

The parameters related to the star are listed in Table 1. They are set to match measured parameters for HD209458, and we use the limb-darkening profile from Knutson et al. (2007b). We normalize the flux to that of a blackbody of temperature T_* of the size and at the distance of HD209458.

3.2. Parameters of the Planet

The parameters related to the planet are in Table 2. We model the planet as an inner component that is essentially a billiard ball (completely opaque at all wavelengths) and an outer component that is an isothermal atmosphere with scale height $H = R_{\text{gas}}T_p/\mu g$, where R_{gas} is the gas constant, μ is the molar mass, and g is the acceleration of gravity. The density of our model planet’s atmosphere varies as $\rho = \rho_0 \exp[(r - R_{p0})/H]$, where R_{p0} is the radius of the optically thick part (some authors have called this radius the “cloud–deck” (Charbonneau et al. 2002)). This hypothetical cloud deck could cause the planet to be optically thick at a higher altitude than would otherwise be expected, as discussed in, e.g., Richardson et al. (2003) and Sudarsky et al. (2000). The cloud deck causes the optical depth as a function of radius in our model to have a singular discontinuity at radius R_{p0} .

3.3. Spectral Parameters

The parameters pertaining to the shape of the observed spectrum are in Table 3. In addition to the location of the planet within the stellar disk, the shape of the stellar spectrum and the wavelength–dependent opacity of the planet’s atmosphere together influence the transmission spectrum.

`Spec_Shape` is a parameter that can take on the values “Flat”, “Blackbody”, or “Solar”, and determines the rest–frame spectrum of the model stellar photosphere. (The integrated stellar spectrum is the convolution of the rest–frame spectrum with the stellar rotation profile.) When “Flat” is chosen, the rest–frame model stellar spectrum intensity is set to the mean value of the blackbody intensity in the specified wavelength range $[\lambda_{\text{min}}, \lambda_{\text{max}}]$, which, in our simulation, is set to [580 nm, 600 nm]. When “Solar” is chosen, the model stellar spectrum intensity is set to a high–resolution solar spectrum that is normalized to the flux

Table 1. Model Transit Parameters: Star

Parameter	Description	Value
M_*	Star Mass	$1.05 M_{\odot} = 2.09 \times 10^{33} \text{ g}$
R_*	Star Radius	$1.05 R_{\odot} = 7.35 \times 10^{10} \text{ cm}$
T_*	Star Temperature	6100 K
d_*	Distance to star	47 pc
τ_*	Stellar Rotation Period	1 month

from HD209458⁴; but the Na D lines in this high-resolution spectrum have been replaced by Gaussian fits to the solar lines.

The planet’s atmosphere has N_{abs} absorption features, each of which is due to an element with a given fraction of the solar abundance. In the models presented in this paper, $N_{\text{abs}} = 2$: we consider the Na doublet at 588.9950 nm and 589.5924 nm, with sodium at fractional abundance $f_{\odot} \equiv X_{\text{Na } p}/X_{\text{Na } \odot} = 0.01$ of the solar abundance. Each line is modeled as a Voigt profile, as described in, e.g., Press & Rybicki (1993).

3.4. Parameters of Observing and Computing

The final set of parameters, listed in Table 4, includes those that specify the observer and those that determine how the observation is discretized for the purpose of numerical computation. The model observational setup is determined by three parameters: the telescope’s diameter D (6 m in our simulations) and efficiency η (100%), and the spectrograph’s spectral resolution R_S (we set R_S to 700,000 for the purpose of computing the model, and we re-bin to lower, more easily achieved resolutions – 150,000 and 50,000 – after computing a model). These three parameters prescribe the sizes of the spectral bins and the rate at which those bins are capable of collecting light.

In order to compute the flux at Earth as a function of wavelength, we begin by dividing the stellar disk into n_{b*} concentric annuli, and we divide each annulus into $n_{\phi*}$ azimuthal sections. In each section, the redshifted spectrum and the normalization must both be computed.

Knowing the stellar rotation rate and axis, we may calculate the recessional velocity of any point on the star’s surface as a function of its location on the projected stellar disk, and we redshift the spectrum from each part of the star accordingly. When the planet is in-transit, we separate the stellar disk into an annulus that contains the planet and the rest of the disk that we treat as described above. The annulus that contains the planet is treated almost as above – divided into n_{b*A} sub-annuli, each of which has $n_{\phi*A}$ azimuthal sections – but the sub-annuli are incomplete, interrupted by the planet.

In order to sample the planet’s atmosphere, we divide the region that overlaps the star into n_{bp} concentric annuli around the planet’s center, each of which is divided into $n_{\phi p}$ azimuthal sections. In each section, we must determine the optical depth and multiply by $\exp(-\tau)$. In calculating the optical depth, we note that in the case that the planet’s rotation axis is entirely normal to the line-of-sight, if the planet rotates as a solid body then the

⁴From <ftp://solarch.tuc.noao.edu/>.

Table 2. Model Transit Parameters: Planet

Parameter	Description	Value
M_p	Planet Mass	$0.69M_J = 1.31 \times 10^{30}$ g
R_{p0}	Optically Thick Planet Radius	$1.32R_J = 9.44 \times 10^5$ km
P_0	Planet Pressure at R_{p0}	0.01 bars
H	Planet Atmosphere Scale Height	500 km
T_p	Planet Atmosphere Temperature	1300 K
f_{TL}	Frac. Tidal Locked Rot. Rate	0 or 1 ($v_{\text{eq}} = 0$ or 2 km s ⁻¹)
a	Semi-Major Axis	0.046 AU
$\#_H$	Number of Scale Heights in Atm.	15

^aParameter values are set to match measured values from the HD209458b system where possible.

Table 3. Model Transit Parameters: Spectral Features

Parameter	Description	Value
Spec_Shape	Shape of Star Spectrum	Flat, Blackbody, or Solar
λ_{min}	Min. Wavelength in Sim.	580 nm
λ_{max}	Min. Wavelength in Sim.	600 nm
N_{abs}	# Abs. Features in P. Atm.	2
$f_{\odot 1}$	Frac. Solar Abund., First Line	0.01
λ_{01}	First Line–Center	588.9950 nm
A_{ki1}	Transition Prob. First Line	6.16×10^{-9} s ⁻¹
g_{i1}	Stat. Wt. Lower Level First Line	2
g_{k1}	Stat. Wt. Upper Level First Line	4
$f_{\odot 2}$	Frac. Solar Abund., Second Line	0.01
λ_{02}	Second Line–Center	589.5924 nm
A_{ki2}	Transition Prob. Second Line	6.14×10^{-9} s ⁻¹
g_{i2}	Stat. Wt. Lower Level Second Line	2
g_{k2}	Stat. Wt. Upper Level Second Line	2

^aIn parameters that have i and k subscripts, i indicates the lower level ($3s_{1/2}$ for both lines) and k indicates the upper level ($3p_{3/2}$ for the bluer line and $3p_{1/2}$ for the redder line). The fractional solar abundance is set to 0.01 in order to achieve modest agreement with data observed for the Na D doublet in HD209458b’s atmosphere.

radial component of its recessional velocity is constant along a ray:

$$\tau[b_p, \phi, \lambda] = N[b_p] \times \sigma \left[\frac{\lambda}{1 + (v_p[b_p, \phi_p]/c)} \right], \quad (8)$$

where the column density is calculated in terms of a function G that is specified below: $N[b_p] = n_0 G[b_p, R_{p0}, H]$. In equation (8), $v_p[b_p, \phi_p]$ is the recessional velocity of the planet, as a function of radius and azimuth, which depends upon the orbit and the rotation. Note that there is a single v_p along a given line-of-sight defined by a (b_p, ϕ_p) pair only under the assumption of solid body rotation. The rest-frame cross-section $\sigma[\lambda]$ is computed according to the Voigt profile. The function G is defined as the following integral:

$$G[b_p, R_{p0}, H] = \begin{cases} \int_{-\infty}^{\infty} \exp \left[-\frac{\sqrt{b^2 + l^2} - R_{p0}}{H} \right] dl & b_p > R_p \\ \infty & b_p \leq R_p \end{cases}. \quad (9)$$

4. Model Transit Spectra

As described in § 2.2, we seek the expected signal-to-noise ratio for distinguishing between the spectrum that would be observed due to a non-rotating planet (or one that is in a Cassini state with its rotation axis nearly in the plane of orbit) and the spectrum that would be observed due to a tidally locked planet. The computed model spectrum $\mathcal{N}[\lambda]$ is the time integral of the instantaneous spectrum $\dot{\mathcal{N}}[\lambda]$ and consists of the number of photons detected per wavelength bin:

$$\mathcal{N}[\lambda] \approx \dot{\mathcal{N}}[\lambda] \Delta t_{\text{obs}},$$

for some small exposure time Δt_{obs} .

The model signal (of rotation) per bin that we are looking for is the difference between the rotating model spectrum \mathcal{N}_{rot} and the non-rotating model spectrum $\mathcal{N}_{\text{no rot}}$:

$$S_b = \left(\dot{\mathcal{N}}_{\text{rot}}[\lambda] - \dot{\mathcal{N}}_{\text{no rot}}[\lambda] \right) \Delta t_{\text{obs}}. \quad (10)$$

We make the optimistic approximation that the noise per bin is just the photon-noise:

$$N_b = \sqrt{\dot{\mathcal{N}}_{\text{no rot}}[\lambda] \Delta t_{\text{obs}}}. \quad (11)$$

The total signal-to-noise ratio in a single exposure, then, is the sum in quadrature of S_b/N_b for all wavelength bins λ_i :

$$S/N = \sqrt{\sum_{i=1}^{\#\text{bins}} \left(\frac{\dot{\mathcal{N}}_{\text{rot}}[\lambda_i] - \dot{\mathcal{N}}_{\text{no rot}}[\lambda_i]}{\sqrt{\dot{\mathcal{N}}_{\text{no rot}}[\lambda_i]}} \right)^2} \times \sqrt{\Delta t_{\text{obs}}}. \quad (12)$$

A similar summation in quadrature applies over all exposures. Note that, in principle, the expression in equation (12) is insensitive to the sizes of bins and hence to the spectral resolution R_S , as long as the bins are small relative to the Gaussian width of the absorption feature under consideration. Our simulations indicate that the spectral resolution must be $\gtrsim 500,000$ in order for S/N to be nearly independent of R_S .

The effect of rotation, both during ingress and during mid-transit, is illustrated in Figure 2. For illustrative purposes, in this figure we assume a uniform star (flat spectrum, non-rotating, no limb-darkening). On the left panels of Figure 2, we show a snap-shot during ingress (at 1.5th contact) and on the right, we show a snap-shot during the middle of a transit (2.5th contact). The quantity plotted is $\mathcal{R}' = \mathcal{R} - 1$ from B01, where

$$\mathcal{R}[\lambda, t] = \frac{\dot{N}_{\text{in transit}}[\lambda, t]}{\dot{N}_{\text{out of transit}}[\lambda, t]} \quad (13)$$

The bottom panels of Figure 2 show the difference spectra between the models with a tidally locked planet and the models with a non-rotating planet ($\mathcal{R}_{\text{rot}} - \mathcal{R}_{\text{no rot}}$).

As described in § 2 above, a planet’s rotation causes the centroids of stellar absorption features to shift relative to a non-rotating planet. In Figure 3, centroid shifts (in velocity units) are plotted as a function of position in transit, for a planet transiting in front of a realistic star model with a Sun-like spectrum. The recessional velocity increases roughly sinusoidally during ingress, reaching a peak of about 60 cm s^{-1} at 1.5th contact. During mid-transit, between 2nd and 3rd contacts, the net velocity shift is much smaller. Egress is nearly perfectly symmetrical with ingress, though the velocity shifts have the opposite sign.

The cumulative and incremental signal-to-noise ratio across the transit are shown in the top and bottom panels, respectively, of Figure 4. As a planet proceeds in its transit from first contact to fourth contact, the S/N builds up steadily throughout the transit, as can be seen in the top panel of this figure. This cumulative increase reflects the steady incremental S/N per second of observation, which, for a planet crossing in front of a uniform star, is shown in the bottom panel. The three curves in the bottom panel represent, in decreasing order of S/N, the incremental S/N curves that are expected for a spectrograph with ultrahigh-resolution (the simulation’s resolution $R_S = 700,000$), for a spectrograph with as high-resolution as bHROS on Gemini ($R'_S = 150,000$), and for a spectrograph with more standard high-resolution ($R'_S = 50,000$). In the top panel, we show the cumulative S/N (assuming the simulation’s resolution) for a planet in front of a uniform star, and for a planet in front of a more realistic sun-like star that rotates once per month, has a limb-darkening profile, and has a solar spectrum. It is apparent in the top panel of Figure 4 that a spectrograph with our simulation’s resolution would see the effect of rotation at $S/N = 7.1\eta^{1/2}$ in a single transit in the case of the simplified uniform star, and at $S/N = 3.2\eta^{1/2}$ in one transit of the realistic star. The effect of including in the simulation the realistic features of stellar rotation, limb-darkening, and a solar spectrum is therefore to depress the S/N of the effect of tidally locked

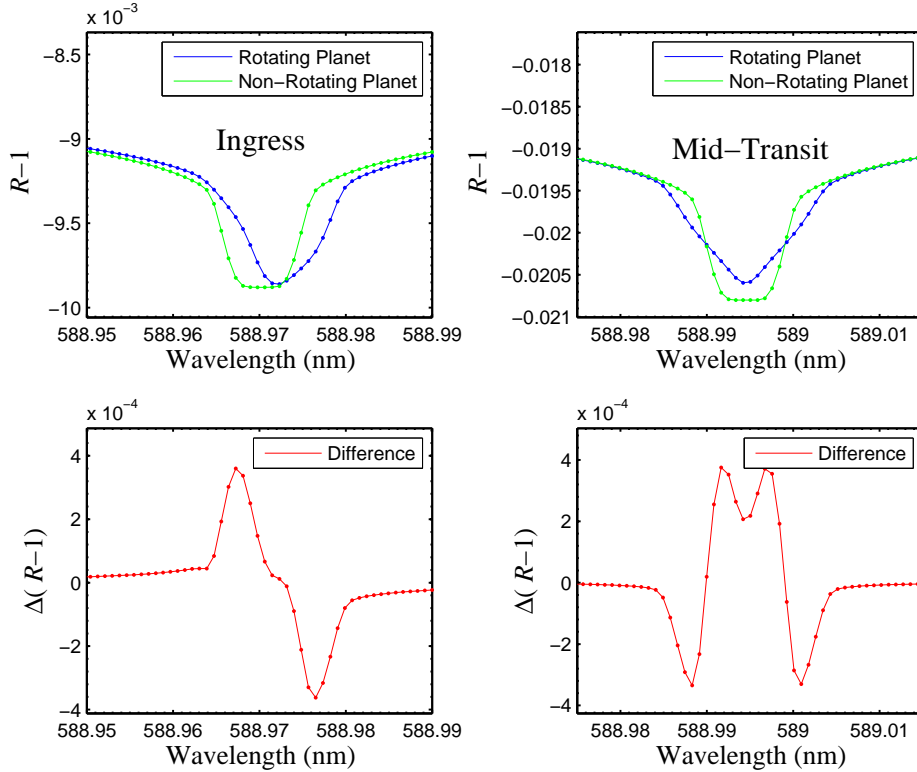


Fig. 2.— Upper panels show snap–shot spectra for one of the the Na D lines for two different model planets (tidally locked and non–rotating); lower panels show the difference between the two model spectra. The quantities plotted are $\mathcal{R}' = \mathcal{R} - 1$ (upper panels) and $\Delta\mathcal{R}'$ (lower panels), where $\mathcal{R}[\lambda, t] = \dot{N}_{\text{in transit}}[\lambda, t] / \dot{N}_{\text{out of transit}}[\lambda, t]$. In the upper panels, the blue curve is the tidally locked planet’s transit spectrum, and the green curve is the non–rotating planet’s transit spectrum. In the lower panels, the difference between the rotating and non–rotating planet’s spectra. *Left*: Halfway through ingress (at 1.5th contact). *Right*: Halfway through the whole transit (2.5th contact).

rotation by a factor of slightly more than 2. The bottom panel of the figure indicates that our predicted S/N for one transit of a realistic star ($3.2\eta^{1/2}$) might be adjusted downward by $\sim 50\%$, depending on the spectral resolution, indicating a total one–transit S/N for the case of the realistic star of about $\sim 1.7\eta^{1/2}$. Finally, we do not show the incremental S/N for the realistic star model, but, as the top panel of the figure indicates, a larger proportion of the total signal comes from ingress and egress in the realistic star model than in the uniform star model.

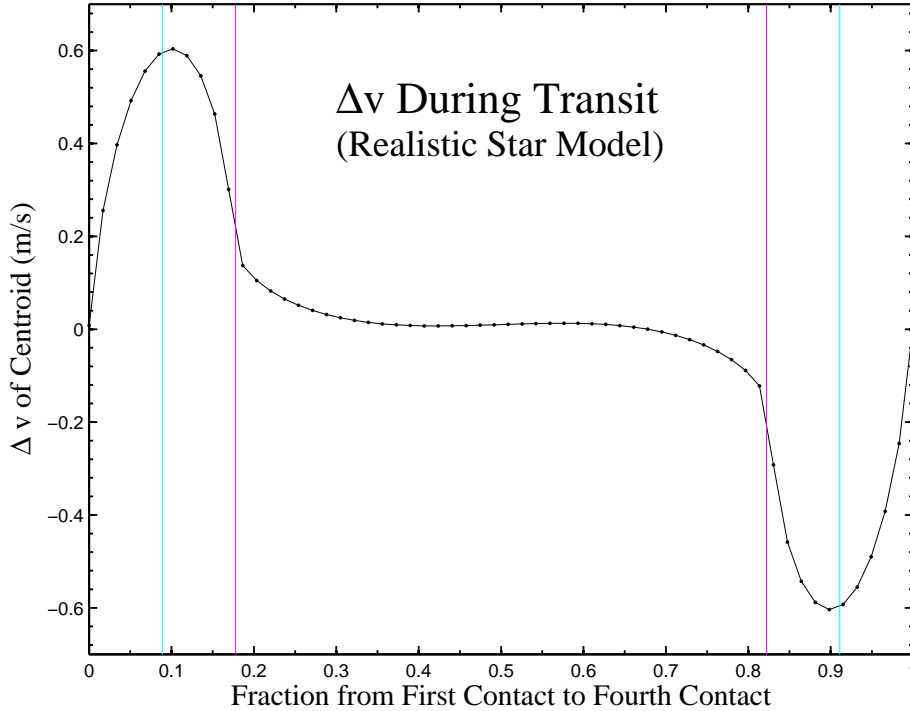


Fig. 3.— Centroid–shift of Na D lines from tidally locked rotation from the beginning to the end of a transit, relative to an identical but non–rotating planet; Sun–like stellar spectrum. The vertical lines denote 1.5th and 3.5th contact (cyan) and second and third contact (magenta). Between first and second contact, the spectrum with the rotating planet is redshifted relative to the non–rotating planet by up to about 60 cm s^{−1}; between third and fourth contact, it is blueshifted by the same amount. This plot samples the transit at 60 regularly–spaced points. Parameters were chosen to represent the HD209458 system.

5. Discussion

The S/N scales with the square root of the number of absorption lines under consideration, with the square root of the number of transits, and with several other parameters, as follows:

$$\begin{aligned}
 S/N \sim & \left(\sqrt{\frac{N_{\text{abs}}}{2}} \right) \left(\sqrt{\# \text{ transits}} \right) \left(\frac{D\sqrt{\eta}}{6 \text{ m}} \right) \times \\
 & 10^{-0.2(V_* - V_0)} \times \left(\frac{R_*}{R_0} \right)^{-2} \left(\frac{R_p H}{R_{p0} H_0} \right) \left(\frac{v}{2000 \text{ m s}^{-1}} \right) \times \\
 & (\psi [R'_S]) (S/N)_0
 \end{aligned} \tag{14}$$

In this equation, N_{abs} is the number of absorption lines, D is the telescope’s diameter, η is the efficiency of the instrumental setup, V_* is the star’s magnitude, V_0 is HD209458’s magnitude (about 7.6), R_* is the stellar radius, R_0 is HD209458’s radius, R_p and H are the planet’s

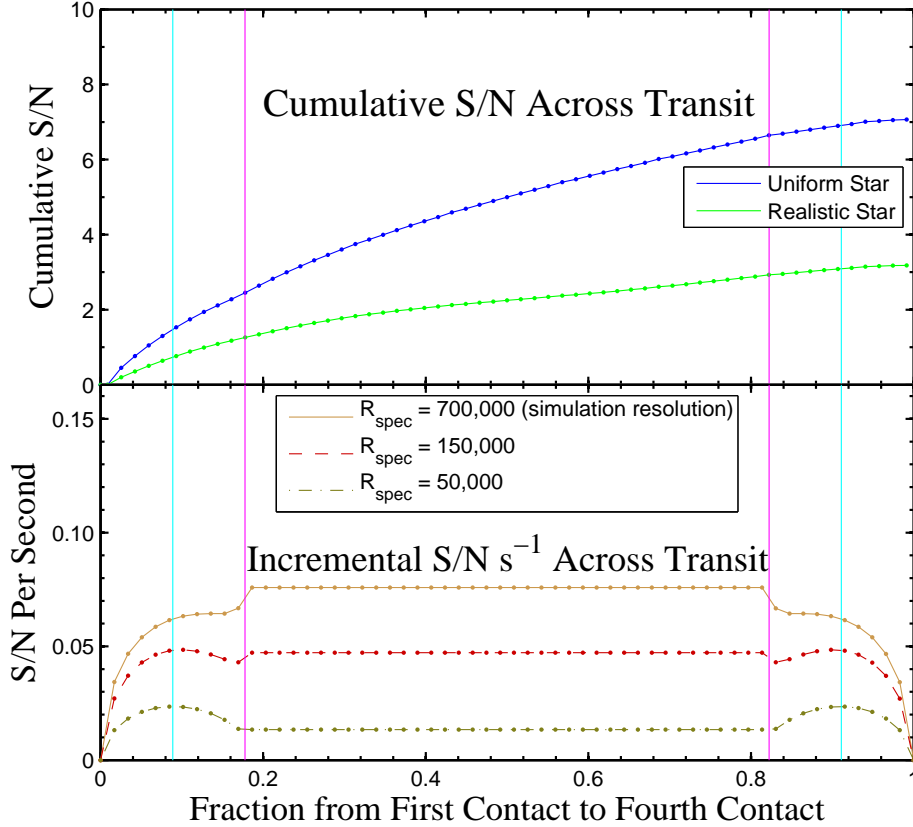


Fig. 4.— *Top*: S/N for distinguishing between a rotating and a non-rotating planet, accumulated during a single transit. Upper curve displays the cumulative S/N for the distinction of a tidally locked planet from a non-rotating model, assuming a completely uniform star: the model star has a flat spectrum, is not rotating, and there is no limb-darkening. Lower curve displays the same, but for a more realistic star: the model star rotates once per month, has the limb-darkening profile determined by Knutson et al. (2007b), and has a solar spectrum. These curves assume the spectral resolution used in the simulation ($R_S = 700,000$); for more easily achievable spectral resolution, these curves are adjusted downward by 30% - 80%, as displayed in the bottom panel. The vertical lines denote 1.5th and 3.5th contact (cyan) and second and third contact (magenta). Also, both top and bottom panels show model results assuming 100% throughput efficiency ($\eta = 100\%$). In practice, these curves would be adjusted downward by a factor $\eta^{1/2}$, or $\sim 0.04^{1/2} = 0.2$ for an ultrahigh resolution spectrograph. *Bottom*: Incremental S/N for sixty 1-second observations across the transit, assuming a uniform, non-rotating star with a flat spectrum. Top curve shows the incremental S/N, assuming a spectrograph with the spectral resolution of the simulation ($R_S = 700,000$). Middle and bottom curves show the same, assuming spectral resolutions $R'_S = 150,000$ and $R'_S = 50,000$, respectively. Parameters of the system (except for the stellar spectrum in the bottom panel) were chosen to represent the HD209458 system.

radius and scale height, and R_{p0} and H_0 are HD209458b’s radius and scale height. $\psi[R'_S]$ is a function that characterizes the (nonlinear) response of S/N to the spectral resolution of the spectrograph; for instance, $\psi[700,000] \approx 1$, $\psi[150,000] \sim 0.6$ and $\psi[50,000] \sim 0.2$. Finally, $(S/N)_0 = 7.1$ for a uniform star and $X_{\text{Na } p}/X_{\text{Na } \odot} = 0.01$; and $(S/N)_0 = 3.2$ for a more realistic (rotating, limb-darkened) star with a solar spectrum.

Culling the signal from mid-transit, however, is much more difficult than from ingress and egress, because the shape of the distortion depends more sensitively on the structure of the planet. For the realistic star, our model predicts $S/N \sim 1.3\eta^{1/2}$ (with the 6 m telescope, with Poisson-dominated photon noise) for ingress alone, and therefore a factor $2^{1/2}$ greater, or $S/N \sim 1.8\eta^{1/2}$ for ingress and egress.

In Table 5, we present the number of orbits that must be observed in order to make a 5σ detection of rotation, for various combinations of parameters. In all cases, we assume a realistically achievable optical setup, with spectral resolution $R'_S = 150,000$ and throughput $\eta = 4\%$. Improvement in R'_S will yield a modest improvement in S/N, and improvement in η could be quite significant. In the third column of Table 5 (A), we present the total available S/N for the whole transit, according to our model, while in the fourth column (B), we present the available S/N from just ingress and egress. The fifth and sixth columns are based on the S/N in the fourth column.

Finally, as a sanity check, our model can be tested by comparing it to the analysis of Charbonneau et al. (2002). That analysis suggests that the sodium content of a planet’s atmosphere can be determined by comparing the flux in a narrow band centered on the sodium resonance lines with the flux in a wider band surrounding but excluding the lines. In that paper, the decrement in the narrow band containing the sodium features is named n_{Na} , and was measured to be -2.32×10^{-4} for HD209458 during the middle of transit. They presented several models, all of which over-predicted the sodium decrement. The model that predicted the smallest magnitude of the decrement had 1% solar metallicity and cloud deck at 0.0368 bar; this model predicts $n_{\text{Na}} \sim -3.4 \times 10^{-4}$ in mid-transit. Our model (1% solar metallicity, cloud deck at 0.01 bar) predicts $\sim -4.1 \times 10^{-4}$ in mid-transit, as shown in Figure 5. We conclude that our model is in reasonable agreement with both Charbonneau et al.’s model ($\sim 20\%$) and with the actual data ($\sim 40\%$).

6. Conclusion

Our investigation indicates that, with currently available instruments, it will be difficult to obtain the sensitivity needed to achieve a minimal $S/N \gtrsim 5$ detection of tidally locked rotation of the planet HD209458b. Nevertheless, it appears that the effect of rotation will have significant (though small) influence on transit-spectra taken with current or near-future instruments. Because this influence is so small, it is worth considering ways that the S/N could be improved, according to the scalings summarized in equation (14).

Table 4. Model Transit Parameters: Observation and Computing

Parameter	Description	Value
D	Telescope Diameter	2.4 m – 30 m
η	Spectroscope Efficiency	1.00
R'_S	Obs. Spec. Resolution	50,000 - 700,000
\mathcal{T}_{int}	Integration Time	932.088 s
R_S	Comp. Spec. Resolution	700,000
Δt	Time-Step in Integration	50 s
n_{b*}	# of Star Annuli	10
$n_{\phi*}$	# of Star Azimuthal Sections	16
n_{b*A}	# of S. Annuli in P. Annulus	10
$n_{\phi*A}$	# of S. Azim. Sec.'s in P. Ann.	10
n_{bp}	# of Planet Atm. Annuli	20
$n_{\phi p}$	# of Planet Atm. Azim. Sections	20

^aParameter values are set to match measured values from the HD209458b system where possible.

Table 5. Required Number of Transits For 5σ Detection

Spec_Shape	D	(S/N)/Tr. (A)	(S/N)/Tr. (B)	Req. # Transits (A)	Duration (A)
Flat (uniform star)	6 m	1.1	0.52	~ 25	~ 3 months
Solar	6 m	0.48	0.27	~ 110	~ 1.25 years
Solar	10 m	0.79	0.45	~ 40	~ 5 months
Solar	30 m	2.4	1.3	~ 5	~ 3 weeks

^aA table showing the number of orbits required to achieve a $S/N = 5$ detection of tidally locked rotation of HD209458b, assuming a planetary Na-content that is 1% solar. Assumptions: we are monitoring two spectral lines (the Na doublet) with a spectrograph with resolving power $R'_S = 150,000$, and an efficiency in the optical setup of 0.04. The third column “(S/N)/Tr. (A)” is the S/N per transit, as shown in Figure 4, and the fourth column is the S/N per transit, considering only ingress and egress. The “(A)” in the fifth and sixth columns indicates that the numbers of transits and the required duration are tabulated for S/N values from column three.

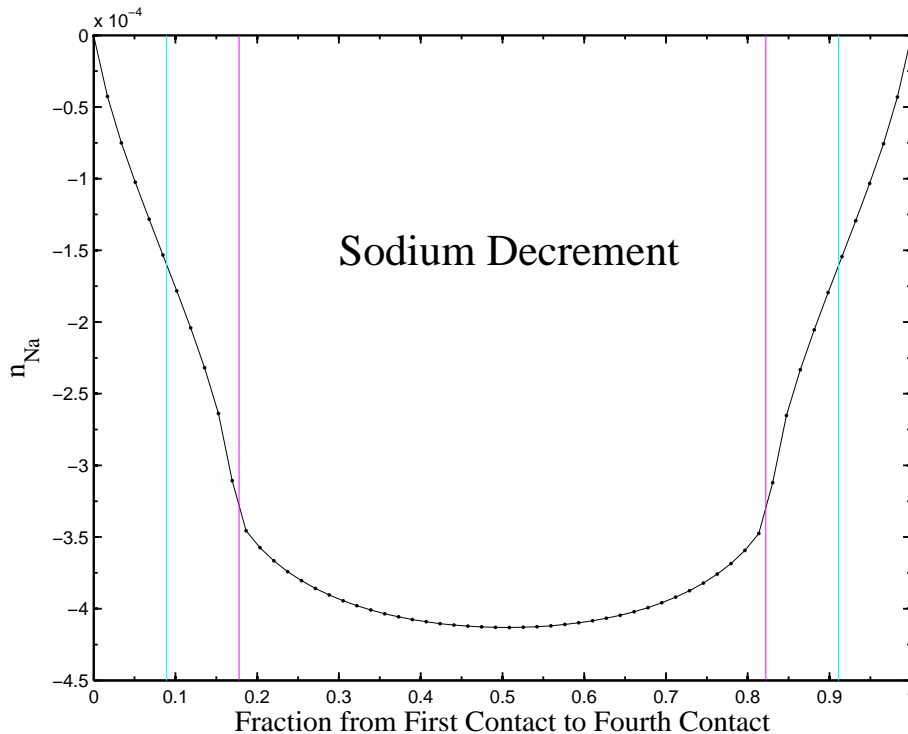


Fig. 5.— The flux decrement due to sodium in the planet’s atmosphere, as shown by the quantity n_{Na} defined by Charbonneau et al. (2002). This decrement reaches a maximum in magnitude of -4.1×10^{-4} , halfway through transit, in our model.

- The most obvious way to boost S/N is to increase the collecting area of the telescope, the effect of which is shown in Table 5. With an extremely large (30 m–class) telescope, the required discrimination power could be achieved in $\sim 5 - 15$ transits, if our optimistic assumptions about the noise are not too far off.
- As the abundances of other elements or molecules in the planet’s atmosphere are identified, the number of absorption lines N_{abs} that can be utilized can increase. Observing four absorption features instead of two will boost the S/N per orbit by $2^{1/2}$ and will therefore cut in half the required observing time to achieve a fixed target S/N .
- The HD189733 system is only 19.3 pc away (Bouchy et al. 2005b), but the star is smaller and dimmer than HD209458, and has the same apparent magnitude. We find that, overall, it has no relative advantage in terms of S/N . It may be unlikely that a star significantly brighter than HD209458 will be found to have a transiting giant planet companion, but if this should happen the signature of rotation will be more readily apparent in the system with the brighter star.
- Finally, since S/N is proportional to the size of the atmosphere, represented by δ_{atm} in equation (7), a planet with a more extended atmosphere would show the distortion

due to rotation more readily. The size of the atmosphere depends on the product of R_p and the height of the atmosphere $\Pi_{\text{atm}} \sim 15H$, so the S/N could be increased in the case of a larger planet, a hotter one, or one with lower surface gravity. Unfortunately, although some other planets are somewhat larger, none of the puffer planets that have been discovered so far happen to transit a star as bright as HD209458. If a more bloated planet is found to transit a star as bright as HD209458, such a planet would probably be a more promising target for the type of study described in this paper.

Although the optical transit spectrum of an extrasolar giant planet contains many precious clues regarding the nature of rotation and climate or weather, we emphasize that we have so far addressed only the forward problem: deep, high spectral resolution transit spectra *will* be distorted by HD209458b’s tidally locked rotation, if indeed it is tidally locked. But seeing the effect of rotation in a spectrum and *knowing* that we are seeing the effect of rotation are two very different things. The inverse problem – identifying the rotation rate – will be much more challenging, and is beyond the scope of this paper’s investigation. In brief, it is impossible to decode the clues that the spectrum holds without a Rosetta stone – namely, without already possessing accurate knowledge of abundances in the planet’s atmosphere. We note that when it comes to solving the inverse problem, it may be possible to make do without a perfect Rosetta stone by comparing the star’s spectrum at two different times of transit instead of comparing it to an accurate input model. Specifically, comparing the ingress spectrum to the egress spectrum should eliminate various systematic uncertainties that may affect both ingress and egress spectra. This strategy involves foregoing spectra between second and third contacts, at a cost of a factor of ~ 2 in S/N , but has the advantage of being more robust with respect to errors in modeling the planetary atmosphere. Furthermore, if detailed analysis along the lines of Charbonneau et al. (2002) should reveal many more planetary absorption features, a large current-generation telescope could detect the motion of an extrasolar planet’s atmosphere in of order a month.

A final point to keep in mind is that the technique presented in this paper is not limited to discerning the difference between a tidally locked planet and a non-rotating planet; this technique can be used to investigate the applicability of any model of the motion of a transiting planet’s atmosphere. Some atmospheric circulation models of Hot Jupiters predict extremely fast winds, up to $\sim 9 \text{ km s}^{-1}$, or more than four times the predicted equatorial rotation rate. It might therefore turn out to be easier to detect winds than to detect rotation. Moreover, if an analysis similar to the one described here were to find a deviation from the hypothesis of tidally locked rotation, this would mean that *something* interesting is going on – the planet could be rotating roughly as a solid body but at a different rate; there could be significant non-rotational motion in the atmosphere; or there could be some combination of these phenomena.

We thank Caleb Scharf, Frits Paerels, and Greg Bryan for extremely helpful discussions. We gratefully acknowledge George Rybicki for use of a Voigt profile routine. We acknowledge many helpful comments by our anonymous referee.

REFERENCES

- Alonso, R., Brown, T. M., Torres, G., Latham, D. W., Sozzetti, A., Mandushev, G., Belmonte, J. A., Charbonneau, D., Deeg, H. J., Dunham, E. W., O’Donovan, F. T., & Stefanik, R. P. 2004, *ApJ*, 613, L153
- Bakos, G. Á., Knutson, H., Pont, F., Moutou, C., Charbonneau, D., Shporer, A., Bouchy, F., Everett, M., Hergenrother, C., Latham, D. W., Mayor, M., Mazeh, T., Noyes, R. W., Queloz, D., Pál, A., & Udry, S. 2006, *ApJ*, 650, 1160
- Bakos, G. A., Kovacs, G., Torres, G., Fischer, D. A., Latham, D. W., Noyes, R. W., Sasselov, D. D., Mazeh, T., Shporer, A., Butler, R. P., Stefanik, R. P., Fernandez, J. M., Sozzetti, A., Pal, A., Johnson, J., Marcy, G. W., Winn, J., Sipocz, B., Lazar, J., Papp, I., & Sari, P. 2007a, *ArXiv e-prints*, 705
- Bakos, G. Á., Noyes, R. W., Kovács, G., Latham, D. W., Sasselov, D. D., Torres, G., Fischer, D. A., Stefanik, R. P., Sato, B., Johnson, J. A., Pál, A., Marcy, G. W., Butler, R. P., Esquerdo, G. A., Stanek, K. Z., Lázár, J., Papp, I., Sári, P., & Sipócz, B. 2007b, *ApJ*, 656, 552
- Barman, T. 2007, *ApJ*, 661, L191
- Barnes, J. W. & Fortney, J. J. 2003, *ApJ*, 588, 545
- Bodenheimer, P., Laughlin, G., & Lin, D. N. C. 2003, *ApJ*, 592, 555
- Bouchy, F., Bazot, M., Santos, N. C., Vauclair, S., & Sosnowska, D. 2005a, *A&A*, 440, 609
- Bouchy, F., Pont, F., Santos, N. C., Melo, C., Mayor, M., Queloz, D., & Udry, S. 2004, *A&A*, 421, L13
- Bouchy, F., Udry, S., Mayor, M., Moutou, C., Pont, F., Iribarne, N., da Silva, R., Ilovaisky, S., Queloz, D., Santos, N. C., Ségransan, D., & Zucker, S. 2005b, *A&A*, 444, L15
- Brown, T. M. 2001, *ApJ*, 553, 1006
- Burke, C. J., McCullough, P. R., Valenti, J. A., Johns-Krull, C. M., Janes, K. A., Heasley, J. N., Summers, F. J., Stys, J. E., Bissinger, R., Fleenor, M. L., Foote, C. N., Garcia-Melendo, E., Gary, B. L., Howell, P. J., Mallia, F., Masi, G., Taylor, B., & Vanmunster, T. 2007, *ArXiv e-prints*, 705

- Burrows, A., Hubeny, I., Budaj, J., & Hubbard, W. B. 2007, *ApJ*, 661, 502
- Burrows, A., Hubeny, I., Hubbard, W. B., Sudarsky, D., & Fortney, J. J. 2004, *ApJ*, 610, L53
- Burrows, A., Sudarsky, D., & Hubbard, W. B. 2003, *ApJ*, 594, 545
- Butler, R. P., Marcy, G. W., Williams, E., McCarthy, C., Dosanjuh, P., & Vogt, S. S. 1996, *PASP*, 108, 500
- Chabrier, G. & Baraffe, I. 2007, *ApJ*, 661, L81
- Charbonneau, D., Brown, T. M., Latham, D. W., & Mayor, M. 2000, *ApJ*, 529, L45
- Charbonneau, D., Brown, T. M., Noyes, R. W., & Gilliland, R. L. 2002, *ApJ*, 568, 377
- Cho, J. Y.-K., Menou, K., Hansen, B. M. S., & Seager, S. 2003, *ApJ*, 587, L117
- Collier Cameron, A., Pollacco, D., Street, R. A., Lister, T. A., West, R. G., Wilson, D. M., Pont, F., Christian, D. J., Clarkson, W. I., Enoch, B., Evans, A., Fitzsimmons, A., Haswell, C. A., Hellier, C., Hodgkin, S. T., Horne, K., Irwin, J., Kane, S. R., Keenan, F. P., Norton, A. J., Parley, N. R., Osborne, J., Ryans, R., Skillen, I., & Wheatley, P. J. 2006, *MNRAS*, 373, 799
- Cooper, C. S. & Showman, A. P. 2005, *ApJ*, 629, L45
- Diego, F., Fish, A. C., Barlow, M. J., Crawford, I. A., Spyromilio, J., Dryburgh, M., Brooks, D., Howarth, I. D., & Walker, D. D. 1995, *MNRAS*, 272, 323
- Dravins, D. 1985, in *IAU Colloq. 88: Stellar Radial Velocities*, ed. A. G. D. Philip & D. W. Latham, 311–+
- Fabrycky, D. C., Johnson, E. T., & Goodman, J. 2007, *ArXiv Astrophysics e-prints*
- Fortney, J. J. 2005, *MNRAS*, 364, 649
- Gaudi, B. S. 2005, *ApJ*, 628, L73
- Gaudi, B. S. & Winn, J. N. 2007, *ApJ*, 655, 550
- Ge, J., Angel, J. R. P., Jacobsen, B., Woolf, N., Fugate, R. Q., Black, J. H., & Lloyd-Hart, M. 2002, *PASP*, 114, 879
- Ge, J., van Eyken, J., Mahadevan, S., DeWitt, C., Kane, S. R., Cohen, R., Vanden Heuvel, A., Fleming, S. W., Guo, P., Henry, G. W., Schneider, D. P., Ramsey, L. W., Wittenmyer, R. A., Endl, M., Cochran, W. D., Ford, E. B., Martín, E. L., Israelian, G., Valenti, J., & Montes, D. 2006, *ApJ*, 648, 683

- Gillon, M., Demory, B. ., Barman, T., Bonfils, X., Mazeh, T., Udry, S., Mayor, M., & Queloz, D. 2007, ArXiv e-prints, 707
- Giménez, A. 2006, ApJ, 650, 408
- Goldreich, P. & Peale, S. 1966, AJ, 71, 425
- Grillmair, C. J., Charbonneau, D., Burrows, A., Armus, L., Stauffer, J., Meadows, V., Van Cleve, J., & Levine, D. 2007, ApJ, 658, L115
- Guillot, T. 2005, Annual Review of Earth and Planetary Sciences, 33, 493
- Guillot, T., Burrows, A., Hubbard, W. B., Lunine, J. I., & Saumon, D. 1996, ApJ, 459, L35+
- Guillot, T. & Showman, A. P. 2002, A&A, 385, 156
- Harrington, J., Hansen, B. M., Luszcz, S. H., Seager, S., Deming, D., Menou, K., Cho, J. Y.-K., & Richardson, L. J. 2006, Science, 314, 623
- Henry, G. W., Marcy, G. W., Butler, R. P., & Vogt, S. S. 2000, ApJ, 529, L41
- Howard, R., Gilman, P. I., & Gilman, P. A. 1984, ApJ, 283, 373
- Hui, L. & Seager, S. 2002, ApJ, 572, 540
- Johns-Krull, C. M., McCullough, P. M., Burke, C. J., Valenti, J. A., Janes, K. A., Heasley, J. N., Bissinger, R., Fleenor, M., Foote, C. N., Garcia-Melendo, E., Gary, B. L., Howell, P. J., Mallia, F., Masi, G., Prato, L. A., & Vanmunster, T. 2007, in American Astronomical Society Meeting Abstracts, Vol. 210, American Astronomical Society Meeting Abstracts, 96.05–+
- Knutson, H. A., Charbonneau, D., Allen, L. E., Fortney, J. J., Agol, E., Cowan, N. B., Showman, A. P., Cooper, C. S., & Megeath, S. T. 2007a, Nature, 447, 183
- Knutson, H. A., Charbonneau, D., Noyes, R. W., Brown, T. M., & Gilliland, R. L. 2007b, ApJ, 655, 564
- Konacki, M., Torres, G., Jha, S., & Sasselov, D. D. 2003, Nature, 421, 507
- Konacki, M., Torres, G., Sasselov, D. D., & Jha, S. 2005, ApJ, 624, 372
- Konacki, M., Torres, G., Sasselov, D. D., Pietrzyński, G., Udalski, A., Jha, S., Ruiz, M. T., Gieren, W., & Minniti, D. 2004, ApJ, 609, L37
- Laughlin, G., Wolf, A., Vanmunster, T., Bodenheimer, P., Fischer, D., Marcy, G., Butler, P., & Vogt, S. 2005, ApJ, 621, 1072

- Levrard, B., Correia, A. C. M., Chabrier, G., Baraffe, I., Selsis, F., & Laskar, J. 2007, *A&A*, 462, L5
- Loeb, A. 2005, *ApJ*, 623, L45
- Mayor, M. & Queloz, D. 1995, *Nature*, 378, 355
- McCullough, P. R., Stys, J. E., Valenti, J. A., Johns-Krull, C. M., Janes, K. A., Heasley, J. N., Bye, B. A., Dodd, C., Fleming, S. W., Pinnick, A., Bissinger, R., Gary, B. L., Howell, P. J., & Vanmunster, T. 2006, *ApJ*, 648, 1228
- McLaughlin, D. B. 1924, *ApJ*, 60, 22
- Narita, N., Enya, K., Sato, B., Ohta, Y., Winn, J. N., Suto, Y., Taruya, A., Turner, E. L., Aoki, W., Tamura, M., Yamada, T., & Yoshi, Y. 2007, *ArXiv Astrophysics e-prints*
- O’Donovan, F. T., Charbonneau, D., Mandushev, G., Dunham, E. W., Latham, D. W., Torres, G., Sozzetti, A., Brown, T. M., Trauger, J. T., Belmonte, J. A., Rabus, M., Almenara, J. M., Alonso, R., Deeg, H. J., Esquerdo, G. A., Falco, E. E., Hillenbrand, L. A., Roussanova, A., Stefanik, R. P., & Winn, J. N. 2006, *ApJ*, 651, L61
- Ohta, Y., Taruya, A., & Suto, Y. 2005, *ApJ*, 622, 1118
- . 2006, *ArXiv Astrophysics e-prints*
- Pont, F., Bouchy, F., Queloz, D., Santos, N. C., Melo, C., Mayor, M., & Udry, S. 2004, *A&A*, 426, L15
- Poynting, J. H. 1903, *MNRAS*, 64, A1+
- Press, W. H. & Rybicki, G. B. 1993, *ApJ*, 418, 585
- Richardson, L. J., Deming, D., Horning, K., Seager, S., & Harrington, J. 2007, *Nature*, 445, 892
- Richardson, L. J., Deming, D., & Seager, S. 2003, *ApJ*, 597, 581
- Robertson, H. P. 1937, *MNRAS*, 97, 423
- Rossiter, R. A. 1924, *ApJ*, 60, 15
- Seager, S. & Hui, L. 2002, *ApJ*, 574, 1004
- Seager, S. & Sasselov, D. D. 2000, *ApJ*, 537, 916
- Showman, A. P. & Guillot, T. 2002, *A&A*, 385, 166
- Silva, A. V. R. 2003, *ApJ*, 585, L147

- Sudarsky, D., Burrows, A., & Hubeny, I. 2003, *ApJ*, 588, 1121
- Sudarsky, D., Burrows, A., & Pinto, P. 2000, *ApJ*, 538, 885
- Swain, M. R., Bouwman, J., Akeson, R., Lawler, S., & Beichman, C. 2007, *ArXiv Astrophysics e-prints*
- Tokunaga, A. T., Bond, T., Elias, J., Chun, M., Richter, M., Liang, M., Lacy, J., Daggert, L., Tollestrup, E., Ressler, M., Warren, D., Fisher, S., & Carr, J. 2006, in *Ground-based and Airborne Instrumentation for Astronomy*. Edited by McLean, Ian S.; Iye, Masanori. *Proceedings of the SPIE*, Volume 6269, pp. 62693Y (2006).
- Trilling, D. E., Lunine, J. I., & Benz, W. 2002, *A&A*, 394, 241
- Udalski, A., Pietrzynski, G., Szymanski, M., Kubiak, M., Zebrun, K., Soszynski, I., Szewczyk, O., & Wyrzykowski, L. 2003, *Acta Astronomica*, 53, 133
- Udalski, A., Szewczyk, O., Zebrun, K., Pietrzynski, G., Szymanski, M., Kubiak, M., Soszynski, I., & Wyrzykowski, L. 2002a, *Acta Astronomica*, 52, 317
- Udalski, A., Szymanski, M., Kubiak, M., Pietrzynski, G., Soszynski, I., Wozniak, P., Zebrun, K., Szewczyk, O., & Wyrzykowski, L. 2002b, *Acta Astronomica*, 52, 217
- Udalski, A., Szymanski, M. K., Kubiak, M., Pietrzynski, G., Soszynski, I., Zebrun, K., Szewczyk, O., & Wyrzykowski, L. 2004, *Acta Astronomica*, 54, 313
- Udalski, A., Zebrun, K., Szymanski, M., Kubiak, M., Soszynski, I., Szewczyk, O., Wyrzykowski, L., & Pietrzynski, G. 2002c, *Acta Astronomica*, 52, 115
- Ulrich, R. K. 1991, *Advances in Space Research*, 11, 217
- Vidal-Madjar, A., Désert, J.-M., Lecavelier des Etangs, A., Hébrard, G., Ballester, G. E., Ehrenreich, D., Ferlet, R., McConnell, J. C., Mayor, M., & Parkinson, C. D. 2004, *ApJ*, 604, L69
- Vidal-Madjar, A., Lecavelier des Etangs, A., Désert, J.-M., Ballester, G. E., Ferlet, R., Hébrard, G., & Mayor, M. 2003, *Nature*, 422, 143
- Winn, J. N. & Holman, M. J. 2005, *ApJ*, 628, L159
- Winn, J. N., Johnson, J. A., Marcy, G. W., Butler, R. P., Vogt, S. S., Henry, G. W., Roussanova, A., Holman, M. J., Enya, K., Narita, N., Suto, Y., & Turner, E. L. 2006, *ApJ*, 653, L69
- Winn, J. N., Noyes, R. W., Holman, M. J., Charbonneau, D., Ohta, Y., Taruya, A., Suto, Y., Narita, N., Turner, E. L., Johnson, J. A., Marcy, G. W., Butler, R. P., & Vogt, S. S. 2005, *ApJ*, 631, 1215

